Featuring work from Prof. Mohammed Baalousha at the Center for Environmental Nanoscience and Risk, Department of Environmental Health Sciences, Arnold School of Public Health, University of South Carolina, United States.

Discovery and potential ramifications of reduced iron-bearing nanoparticles—magnetite, wüstite, and zero-valent iron—in wildland–urban interface fire ashes

Fires at the wildland-urban interface alter the speciation of iron oxides resulting in the formation of reduced iron-bearing nanomaterials including magnetite, wüstite, and zero valent iron-bearing nanomaterials. Magnetic particles — including maghemite and magnetite — are the dominant iron-bearing nanomaterials in fire ashes.

As featured in:

See Mohammed Baalousha *et al.*, *Environ. Sci.: Nano*, 2022, **9**, 4136.

ROYAL SOCIETY OF CHEMISTRY

rsc.li/es-nano

Registered charity number: 207890

Environmental Science Nano

ROYAL SOCIETY OF CHEMISTRY

PAPER

View Article Online
View Journal | View Issue

Cite this: *Environ. Sci.: Nano*, 2022, **9**, 4136

Discovery and potential ramifications of reduced iron-bearing nanoparticles—magnetite, wüstite, and zero-valent iron—in wildland–urban interface fire ashes†

Mohammed Baalousha, *[a] Morgane Desmau, [b] Sheryl A. Singerling,[c] Jackson P. Webster, [d] Sandrine J. Matiasek, [e] Michelle A. Stern [f] and Charles N. Alpers [f]

The increase in fires at the wildland–urban interface has raised concerns about the potential environmental impact of ash remaining after burning. Here, we examined the concentrations and speciation of iron-bearing nanoparticles in wildland–urban interface ash. Total iron concentrations in ash varied between 4 and 66 mg g^{-1}. Synchrotron X-ray absorption near-edge structure (XANES) spectroscopy of bulk ash samples was used to quantify the relative abundance of major Fe phases, which were corroborated by transmission electron microscopy measurements. Maghemite (γ-$(Fe^{3+})_2O_3$) and magnetite (γ-$Fe^{2+}(Fe^{3+})_2O_4$) were detected in most ashes and accounted for 0–90 and 0–81% of the spectral weight, respectively. Ferrihydrite (amorphous Fe(III)–hydroxide, $(Fe^{3+})_5HO_8{\cdot}4H_2O$), goethite ($\alpha$-$Fe^{3+}OOH$), and hematite ($\alpha$-$Fe^{3+}{}_2O_3$) were identified less frequently in ashes than maghemite and magnetite and accounted for 0–65, 0–54, and 0–50% of spectral weight, respectively. Other iron phases identified in ashes include wüstite ($Fe^{2+}O$), zerovalent iron, FeS, $FeCl_2$, $FeCl_3$, $FeSO_4$, $Fe_2(SO_4)_3$, and $Fe(NO_3)_3$. Our findings demonstrate the impact of fires at the wildland–urban interface on iron speciation; that is, fires can convert iron oxides (*e.g.*, maghemite, hematite, and goethite) to reduced iron phases such as magnetite, wüstite, and zerovalent iron. Magnetite concentrations (*e.g.*, up to 25 mg g^{-1}) decreased from black to gray to white ashes. Based on transmission electron microscopy (TEM) analyses, most of the magnetite nanoparticles were less than 500 nm in size, although larger particles were identified. Magnetite nanoparticles have been linked to neurodegenerative diseases as well as climate change. This study provides important information for understanding the potential environmental impacts of fires at the wildland–urban interface, which are currently poorly understood.

Received 6th May 2022,
Accepted 8th August 2022

DOI: 10.1039/d2en00439a

rsc.li/es-nano

Environmental significance

Fires at the wildland–urban interface have been increasing in frequency, size, and severity, resulting in increased emissions of contaminants, including incidental nanoparticles. This study reports the speciation and concentrations of iron-bearing nanoparticles in wildland–urban interface ashes. Maghemite and magnetite were detected in most ashes and accounted for 0–90 and 0–81% of the spectral weight, respectively. Ferrihydrite, goethite, and hematite were identified less frequently in ashes than maghemite and magnetite and accounted for 0–65, 0–54, and 0–50% of spectral weight, respectively. Other iron phases identified in ashes include wüstite, zerovalent iron, FeS, $FeCl_2$, $FeCl_3$, $FeSO_4$, $Fe_2(SO_4)_3$, and $Fe(NO_3)_3$. These findings suggest that fires convert iron oxides (*e.g.*, maghemite, hematite, and goethite) to reduced iron phases such as magnetite, wüstite, and zerovalent iron. Such transformation of iron phases can have serious environmental and human health effects as magnetite nanoparticles have been linked to neurodegenerative diseases as well as climate change.

[a] *Center for Environmental Nanoscience and Risk, Department of Environmental Health Sciences, Arnold School of Public Health, University of South Carolina, Columbia, South Carolina, USA. E-mail: mbaalous@mailbox.sc.edu*
[b] *Deutsches Elektronen-Synchrotron DESY, Notkestr. 85, 22607 Hamburg, Germany*
[c] *National Center for Earth and Environmental Nanotechnology Infrastructure (NanoEarth), Institute for Critical Technology and Applied Science, Virginia Polytechnic Institute and State University, Blacksburg, Virginia, USA*
[d] *Department of Civil Engineering, California State University Chico, 400 W 1st St, Chico, CA 95929, USA*
[e] *Department of Earth and Environmental Sciences, California State University Chico, 400 W 1st St, Chico, CA 95929, USA*
[f] *U.S. Geological Survey, California Water Science Center, 6000 J Street, Sacramento, CA 95819, USA*

† Electronic supplementary information (ESI) available. See DOI: https://doi.org/10.1039/d2en00439a

1. Introduction

Fire is a natural process that has occurred in many ecosystems worldwide since the evolution of land plants some 250 to 400 million years ago.[7] The crux of the wildfire problem nowadays is the increased fire frequency, size, severity,[8] and the spread of fires into the built environment (*i.e.*, fires at the wildland–urban interface, WUI), resulting in increased emissions of contaminants of emerging concern,[9,10] many of which remain to be discovered. Both known and unknown contaminants from fires threaten ecosystems with implications for air and water pollution and, subsequently, environmental and human health.[11,12] For instance, particulate matter from wildfires is more toxic than equal doses from other sources such as ambient pollution.[13,14] Wildfire smoke impacts respiratory health more than fine particles from other sources.[15,16] Additionally, recent studies have found an association between wildfires and wood smoke exposure to cognitive dysfunction, including Alzheimer's disease and dementia,[17,18] yet it is not clear which contaminants in the wildfire emissions contribute to this disease.

Fire at the WUI transforms fuels (*i.e.*, vegetation, soil organic matter, and construction material) into materials with different chemical and physical properties, including black carbon, methane, carbon monoxide, carbon dioxide and ash.[1] These fire emissions (*e.g.*, black carbon, methane, carbon monoxide) together with the heat generated by the fires render the surrounding environment highly reductive.[2,3] For instance, previous studies demonstrated the reduction of TiO_2 to titanium suboxides (*e.g.*, Magnéli phases) in coal burning power plants.[4,5] Ash is the particulate residue after fire that remains *in situ*, is transported in air, or is deposited on the ground, and consists of minerals and charred organic materials.[1] The quantity and characteristics of ash produced during a fire depend on fuel type, combustion completeness, and burned fuel. Low combustion completeness (low fire severity, *e.g.*, $T < 450$ °C) forms black ash with organic carbon as the main component. At high combustion completeness (high fire severity, *e.g.*, $T > 450$ °C), most organic carbon is volatilized, leaving behind mineral ash (or white ash) with calcium, magnesium, sodium, potassium, silicon, and phosphorus in the form of inorganic minerals, mostly carbonates.[19–21] At combustion temperatures >850 °C, the most common inorganics are oxides, including iron oxides.[1]

In plants, among the various organic Fe compounds, the protein phytoferritin stores iron as a hydrous ferric hydroxide similar to ferrihydrite ($(Fe^{3+})_5O_8{\cdot}4H_2O$),[22,23] which may contribute to pedogenic Fe mineral assemblages in soils.[24,25] Iron stored in ferritin and other organic materials could potentially transform to ferromagnetic phases during the burning of plant material. In man-made structures, iron oxides are widely used as pigment in paints, coatings, and construction material such as concrete products, mortar, paving stones, and roofing tiles. Iron oxide pigments are used as colorants for ceramic glazes, glass, paper, plastic, rubber, and textiles as well as in cosmetics and magnetic ink toner.[26] The total consumption of iron oxide pigments in the United States was approximately 200 000 tons in 2020.[27] $Iron^{3+}$ oxides and hydroxides (*e.g.*, hematite, goethite, and to a lesser degree lepidocrocite) are the most widely used as pigments (*i.e.*, yellow, orange, red, red purplish, and brown).[28] Black pigment uses the mixed Fe^{2+}/Fe^{3+} oxide magnetite.[28]

The combustion of vegetation and structural materials alters the speciation of iron oxides and appears to lead to the formation of magnetite particles. A recent study demonstrated the magnetic properties of plant ashes, which result from the thermal transformation of Fe in both organic and inorganic particulate matter.[29] Another study demonstrated the presence of magnetite (γ-$Fe^{2+}(Fe^{3+})_2O_4$) and/or maghemite (γ-$(Fe^{3+})_2O_3$) particles in burned soils and plants characterized by spherical shapes and sizes typically between 0.1 and 2 μm.[30] The degree of pyrogenic magnetic enhancement of fire-affected soils is strongly related to the wildfire severity. The highest pyrogenic magnetic enhancement is linked to the occurrence of higher severity wildfires in pine forests and is dominated by a superparamagnetic fraction, whereas wildfires of lower severity cause lower pyrogenic enhancement with a larger relative contribution of single-domain ferrimagnetic grains.[30]

Iron-bearing particles in fire ash, particularly magnetite, may have serious implications for human health. Several studies have observed airborne magnetite nanoparticles (NPs) in different human organs, suggesting that magnetite in the atmosphere may be able to enter the human circulatory system or even the brain tissue.[31–33] Exposure of human lung cells to different magnetite size fractions (including NPs) and doses revealed that the studied particles, although being only slightly cytotoxic, led to increased reactive oxygen species formation, mitochondrial damage, and genotoxic effects.[34] The presence of magnetite NPs in the brain is potentially associated with several neurodegenerative diseases, including Alzheimer's and Parkinson's diseases, and oxidative stress appears to play a key role in the pathogenesis of these diseases.[35,36] Additionally, magnetite NPs could have a host of environmental impacts, such as promoting the formation of algal blooms[37,38] as well as contributing to climate change from absorption of solar radiation.[39,40]

Considering the potential health and global climate effects of magnetite particles, it is important to better understand the emission levels and characteristics of magnetite particles from fire emissions at the WUI. In this study, we assess the speciation of iron in ash generated by fires at the WUI. Notably, as an emerging class of particulate pollutants, there have been no previous reports on the occurrence of anthropogenic magnetite particles in WUI fire emissions. Therefore, our results provide important information for understanding the pollution characteristics and health risks of magnetite particles generated from fires at the WUI.

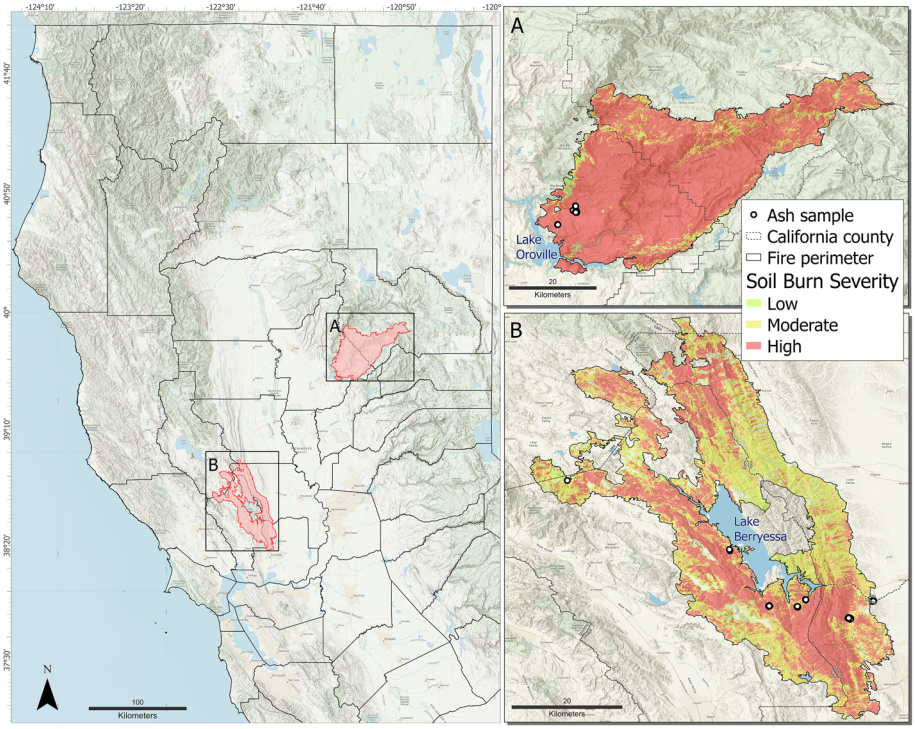

Fig. 1 Map of soil burn severity in the two fires investigated in this study (A) the North Complex (NC) and (B) the LNU Lightning Complex.

2. Materials and methods

2.1. Sampling sites

Two wildland–urban interface fire sites that burned during the 2020 California fire season were examined in this study including the North Complex (NC) Fire, also known as the Bear Fire or the Claremont-Bear Fire and the LNU Lightning Complex Fire (Fig. 1).

North Complex (NC) Fire. This fire, the seventh largest in California history and the second largest recorded in the northern Sierra Nevada, burned 1290 km^2 and destroyed 2455 structures in the Feather River watershed northeast of Lake Oroville, California, between August 17 and December 3, 2020. Lake Oroville is the largest reservoir of the California State Water Project, providing drinking water for more than 23 million of the state's 39 million residents. The west zone of the fire consisted of 342 km^2 located primarily within the Plumas National Forest. Within the fire perimeter, the distribution of burn severity was 2% low, 8% moderate, and 89% high (Fig. 1A).[41,42] The land use within the burned area was 84% evergreen forest, 12% shrub/scrub, and the elevation averaged 1153 m and ranged from 260 to 2132 m (Fig. S1†). The NC Fire burned 28% of the Middle Fork Feather River and 8% of the North Fork Feather River watersheds.

Fire ash and soil samples were collected in the Berry Creek community, where most of the structures were destroyed (Table S1, Fig. S1†). The general setting reflects much of the western slope of the Sierra Nevada in California in the 300–750 m elevation range in terms of geology and vegetation. The area is characterized by steep terrain underlain by granitic and metavolcanic bedrock. The soils vary based on the underlying parent formations with granite forming decomposed granite soil in some areas and the metavolcanic rocks forming "red dirt" soils including the Hartsmill series. At lower elevations *ca.* 300 m, vegetation is characterized by manzanita (*Arctostaphylos* spp.), toyon (*Heteromeles arbutifolia*), interior live oak (*Quercus wislizeni*), California black oak (*Quercus kelloggii*), Pacific poison oak (*Toxicodendron diversilobum*) and very scattered ponderosa pine (*Pinus ponderosa*). At higher elevations *ca.* 750 m, vegetation cover is characterized by California mixed conifers including black and live oaks, Pacific madrone (*Arbutus menziesii*), ponderosa pine, Douglas-fir (*Pseudotsuga menziesii*), and mixed shrub species.

The LNU Lightning Complex Fire. This fire, the sixth largest in California history, burned 1470 km^2 and destroyed 1491 structures in Colusa, Lake, Napa, Sonoma, Solano, and Yolo Counties, approximately 60 km west of Sacramento, between August 17 and October 2, 2020.[43] Within the fire perimeter, the distribution of burn severity was 12% low, 39% moderate, and 49% high (Fig. 1B). Land use in the fire perimeter comprised of 57% shrub/scrub, 19% herbaceous, 12% evergreen forest, and 1.4% developed (Fig. S2†). Roughly half of the Upper Putah Creek watershed was burned and 6.4, 5.5, 4.3, and 3.9% of the upper Cache Creek, Russian River, Suisun Bay, and Lower Sacramento River watersheds burned, respectively. Elevation within the fire footprint was on average 370 m and ranged between 40 and 930 m.

Fire ash samples were collected from vegetated areas and the built environment in Napa and Solano Counties in the vicinity of Lake Berryessa (Table S1, Fig. S2†). The general setting is typical of the Coast Ranges in central California. Elevation of valleys in the Lake Berryessa region generally ranges from 90 to 120 m, with ridge elevations from 600 to 900 m. The geology of the Lake Berryessa region has a diversity of rock types including deformed, metamorphosed sedimentary and volcanic rocks of the Franciscan Complex; sedimentary and volcanic rocks of the Great Valley sequence; igneous rocks of the Clear Lake Volcanics; and alluvium. Soils in the area are typically well-drained and include the Henneke series, formed from weathered, ultramafic rocks such as serpentinite; the Forward series, formed from weathered volcanic rocks; and the Bressa series, formed from weathering of sandstone and shale. Vegetation is diverse in the Lake Berryessa region and varies by elevation. Valley floors typically have grasslands and valley oak woodlands with riparian habitats along creeks and streams; at middle elevations, hardwood forests have various oak species, gray pine, madrone, and chaparral; higher elevations support Douglas-fir, ponderosa pine, incense cedar (*Calocedrus decurrens*), and montane chaparral.

2.2. Sample collection

Fifty-five ash and soil samples were collected during October–November 2020 in the two fire-affected areas (Fig. 1, Table S1†). In the LNU Lightning Complex Fire area, thirty-two ash samples were collected from burned structures and three samples from burned vegetation. In the North Complex area, nine ash samples were collected from burned structures and vehicles, five ash samples from burned vegetation, and six soils affected by fire. In addition, a sample of air-fall ash was collected from a car's windshield during the 2019 fire season. All samples were collected prior to any rain or other precipitation.

The ash samples were collected from various sources including residential structures, garages, vehicles, vegetation, and soils representing low to high burn severity (Table S1†). The burned structures included residences, a convenience store, and storage sheds; burned vehicles included automobiles, tractors, and a boat on a trailer. Vegetation types sampled included oak, pine, manzanita, chamise, and grasses.

Within the LNU Lightning Complex Fire area, undisturbed ash samples were collected from burned structures and vegetation to represent specific location sources; ash samples were collected from multiple locations (*e.g.*, kitchen, living room, bedroom, garage, foundation, *etc.*) within each residential structure; detached structures adjacent to residences (*e.g.*, sheds, barns, and trailers) and a commercial structure (convenience store) were also sampled (Table S1†). Ash samples were collected with disposable plastic scoops and placed into zippered plastic bags.

Within the NC Fire area, ash and soil samples (Table S1†) were collected from around the Madrone Lake Community. Undisturbed ash was scraped from the soil surface and collected to represent average (mixed) sources (Fig. S3†). In burned structures from the NC Fire area, ash collected from multiple locations within the footprint of the structure was combined to form a representative composite sample. Note that sampling burned structures is very difficult because the ash is not uniform like vegetation ash. Structural ash often a mixture of wallboard, insulation, large debris, and combusted material residuals. To collect underlying soil, the area where surface ash was collected was cleared of additional ash and the underlying soil was collected using a plastic scoop from two soil depths (0–2 cm, NC 12B and NC 13B, and 10–15 cm, NC 12C and NC 13C). All samples were collected in acid-washed HDPE wide-mouth bottles.

2.3. Transmission electron microscopy

Transmission electron microscopy (TEM) was used to study the morphology, dimensions, crystallinity, and elemental composition of NPs in a select set of ash samples (A122 and A124). The samples were prepared for TEM analyses by the drop casting method using suspensions of WUI fire ash dispersed in methanol. The suspensions were shaken, left to sit for several minutes, and then dropped onto LC300-Cu-150 TEM grids (Electron Microscopy Sciences), which consist of a lacey carbon support layer attached to a 300-mesh copper grid. The TEM samples were stored in a vacuum desiccator before being analyzed. TEM data were collected at the Nanoscale Characterization and Fabrication Laboratory at Virginia Polytechnic Institute and State University on a JEOL JEM 2100 S/TEM, operated at 200 kV. TEM bright field images were acquired with a Gatan Ultrascan 1000XP CCD camera, whereas selected area electron diffraction patterns were collected with a Gatan Orius 833 slow scan CCD camera. Energy dispersive X-ray spectroscopy (EDS) elemental maps were obtained using a JEOL genuine 60 mm^2 Silicon Drift Detector. For NP phase identification, we used a combination of compositional information from EDS analyses as well as electron diffraction data. For NPs $>$200 nm, we used selected area electron diffraction, but for smaller NPs or those overlapping with adjacent material to a significant extent, we ran fast-Fourier-transforms (FFTs) on high-resolution TEM bright field images, a technique which generates diffraction patterns.

2.4. X-ray absorption spectroscopy

X-ray absorption near edge structure (XANES) analyses were conducted at the Fe K-edge (7112 eV) on the P65 undulator beamline of the Deutsches Elektronen-Synchrotron (HASYLAB/DESY PetraIII, Hamburg, Germany).[44] Incoming photon flux energy was modulated with a Si(111) double crystal monochromator, with an energy resolution of ~0.7 eV at the Fe K-edge, and a beam size of 0.3 × 1.5 mm^2. The

effective suppression of higher harmonics was achieved using Si-plane mirrors.

Around 100 mg of each ash sample was carefully ground, mixed with a small amount of cellulose, and pressed into a pellet. Given the relatively low Fe concentration in most of the ash samples, the absorption of the pellets was too high to obtain a transmission measurement of the reference Fe foil simultaneously to sample measurement. In this manner, Fe foil was measured several times over the course of the experiment to ensure a proper alignment. Over-absorption was corrected using the fluorescence correction module present in Larch.[45]

The data were collected from −150 eV below the edge to +700 eV above with a scan energy increment of ~0.4 eV in continuous mode, at room temperature. The time for each spectrum was 180 seconds and a total of 10 to 30 scans were averaged for each sample. Samples were measured in fluorescence mode. Model compounds were carefully ground with cellulose (2.5% iron), packed in ~1 mm thick pellet with a pressure press, sealed with Kapton™ tape and kept inside a glovebox until measurement for the model compounds sensitive to oxidation. Except for $Fe_2(SO_4)_3$, which is sensitive to reduction under the beam and was measured at 20 K in a He-cryostat, all other model compounds were measured at room temperature, similar to the samples. Spectra were measured in transmission mode using ionization chambers with a path length of 5 cm filled with a mixture of N_2, Ar, and Kr to obtain approximately 15, 50, and 100% absorption for the first, second, and third ionization chambers, respectively. Fe foil reference was measured simultaneously to the model compounds. For energy calibration and alignment, the first inflection point in the first derivative of the adsorption threshold of Fe foil was calibrated to 7112 eV.

Fe K-edge XAS spectra were calibrated, averaged, normalized, analyzed, fitted, and plotted using a series of in-house notebooks written in Python using the Larch[45] and Araucaria[46] libraries, Numpy,[47] SciPy[48] and Matplotlib.[49]

XANES was used to identify the Fe species present in ash. Least-square linear combination fitting (LCF) of the XANES region was performed over an energy range of −20 to +70 eV around 7112 eV. The library of Fe model phases consisted of a mixture of commercial references (<50 nm Fe_2O_3 nanopowder, FeS trace metal basis 99.9% purity, $Fe(NO_3)_3{\cdot}9H_2O$, trace metal basis, 99.95% purity, FeO −10 mesh, ≥99.6% trace metals basis, $FeCl_3$ sublime grade, ≥99.9% trace metal basis, $FeCl_2$ tetrahydrate 99.99% trace metal basis) purchased from Aldrich. Model iron oxide compounds such as goethite, ferrihydrite, magnetite, maghemite and hematite were synthetized[50,51] as summarized in the ESI† section. The XANES spectra for all the model compounds used to fit the ash spectra are presented in Fig. S4.† The spectral weight of the iron oxide phases and oxidation states in the ashes are summarized in Table S2.†

To assess the collinearity between the spectra of the Fe model compounds library and to ensure a well-conditioned basis set for LCF, we used the condition number.[52,53] The chi-square metric was used to estimate the goodness of the LCF analysis (Table S2†). To include a reference in the fit, the amount of the model compounds must be superior to 10% and improve the quality of the fit by at least 20%. The uncertainties on the percentage of the distribution obtained by LCF were calculated using the Imfit library.[54]

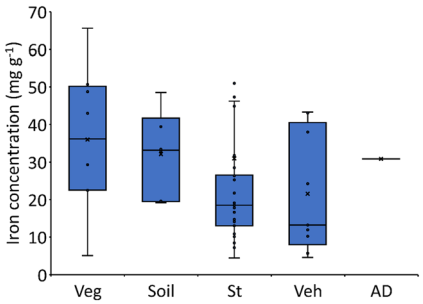

Fig. 2 Total iron concentration in wildland–urban interface ash. Veg: vegetation, St: structure, Veh: vehicle, and AD: atmospheric deposition.

3. Results

3.1. Elemental analysis

The total Fe concentration in the ash samples varied between 4 and 66 mg g^{-1}, except one ash (A092) which had a much higher Fe content of 321 mg g^{-1} (Fig. 2). The median Fe concentration decreased in the following order: vegetation ash 36.1 mg g^{-1} (range: 5.1 to 65.6 mg g^{-1}) > soils 33.1 mg g^{-1} (range: 19.2 to 48.5 mg g^{-1}) > structural ash 18.5 mg g^{-1} (range: 4.5 to 51.0 mg g^{-1}) with one sampling

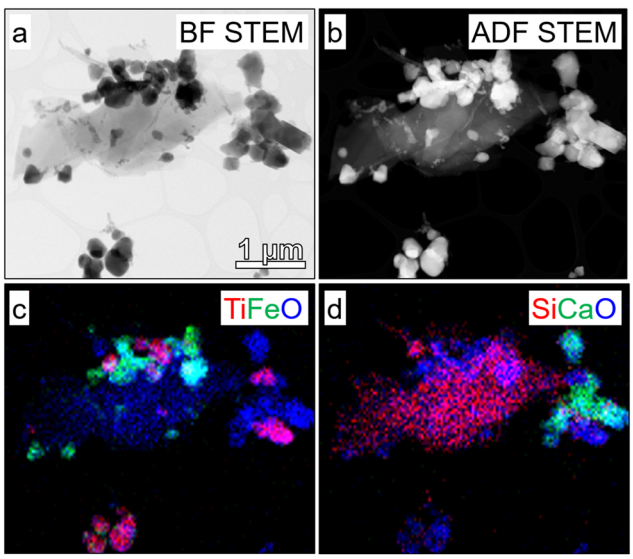

Fig. 3 TEM images and EDS maps illustrating maghemite/magnetite nanoparticles in an aggregate from ash A124. The aggregate's overall morphology is shown in (a) bright field (BF) and (b) annular dark field (ADF) scanning TEM images, whereas compositional information is presented in two composite EDS maps—(c) Ti in red, Fe in green, and O in blue and (d) Si in red, Ca in green, and O in blue.

having an exceptionally high Fe concentration of 321 mg g^{-1} > vehicle 13.2 mg g^{-1} (range: 4.6 to 43.3 mg g^{-1}). Thus, the majority of iron entering the environment following fires likely originates from wildland fuels.

3.2. Transmission electron microscopy analysis

Nanoparticles with various elemental compositions (*e.g.*, Cr, Cu, Fe, Ti) were identified in ash samples A122 and A124. Other metal/metal oxide NPs such as Zn- and Mn-bearing NPs were also identified in other ash samples but are not discussed here. Ash A122 contains Cr-, Cu-, Fe-, and Ti-bearing NPs. Their size (listed as the longest dimension for a particle) ranges are as follows: 180 to 270 nm (n = 3) for Cr-bearing NPs, 10 to 50 nm (n = 13) for Cu-bearing NPs, 190 to 270 nm (n = 2) for Fe-bearing NPs, and 40 to 250 nm (n = 18) for Ti-bearing NPs. Ash A124 contains Cr-, Fe-, and Ti-bearing NPs, with size ranges: 90 to 140 nm (n = 2) for Cr-bearing NPs, 280 to 1070 nm (n = 6) for Fe-bearing NPs, and 190 to 440 nm (n = 13) for Ti-bearing NPs. Fig. 3 shows an example of NPs observed in ash A124. The aggregate consists of an aluminum silicate, calcium carbonate, six Fe-bearing NPs, and thirteen Ti-bearing NPs. For the current study, we focused on the mineral phase identification of the Fe-bearing NPs. Electron diffraction data on the Fe-bearing NPs in ash A124 are consistent with maghemite and/or magnetite. An example of a Fe-bearing NP with its associated diffraction data is shown in Fig. 4. Measurements of the *d*-spacings values of the diffraction spots yielded 8.057, 4.041, 2.707, and 2.549 Å, corresponding to the (100), (200), (300), and (131)

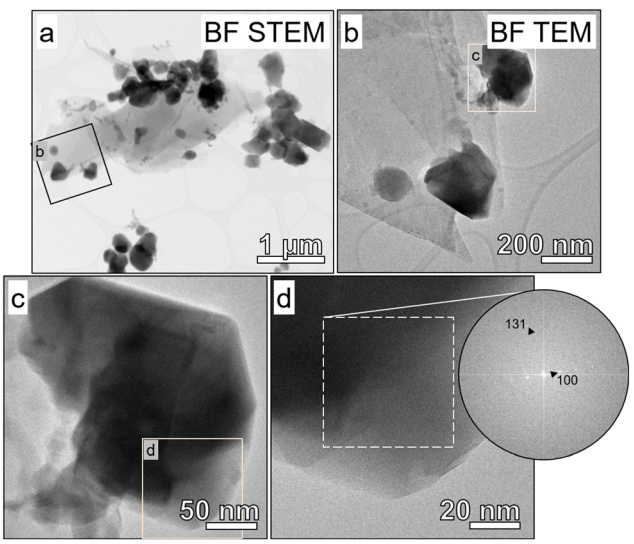

Fig. 4 (a–d) TEM images and an electron diffraction pattern from maghemite/magnetite nanoparticles in an aggregate from ash A124. The images are shown in increasing magnification with the location of the higher magnification images included as insets. A high-resolution bright field (BF) TEM image is shown in (d) with lattice fringes visible. An FFT was performed on the region outlined in white, with the resulting electron diffraction pattern included. It matches [013] for both magnetite and maghemite.

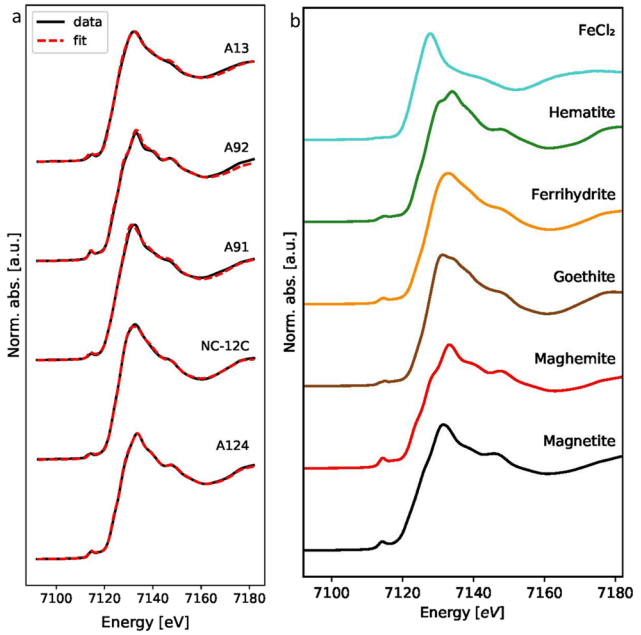

Fig. 5 Example of iron K-edge XANES spectra of (a) fire ash samples and their linear combination (LC) best fits, and (b) the model compounds present in the selected ashes. The ash samples include A124: a structural gray ash, NC-12C: a soil red ash, A091, a structural red ash, A092, a structural black ash, and A013: a structural black ash.

lattice planes of maghemite or magnetite. Maghemite and magnetite have very similar structures and interatomic distances, and thus, are often difficult to distinguish from each other by electron diffraction. However, maghemite is only composed of Fe^{3+} whereas 1/3 of Fe in magnetite is Fe^{2+}. Thus, it is possible to determine the presence of either magnetite or maghemite using XANES.[55]

3.3. Bulk X-ray absorption near edge spectroscopy

The total bulk XANES of representative ash and soil samples are presented in Fig. 5a. The bulk XAS spectra provide an estimate of the weighted atomic average of all major Fe species present in the sample at more than 10%. Spectra were dominated (*e.g.*, >50%) by different Fe components such as ferrihydrite (amorphous hydrous ferric oxide), maghemite, magnetite, goethite (α-$Fe^{3+}OOH$), and hematite (α- $Fe^{3+}{}_2O_3$, Fig. 5b). Other phases such as $FeCl_3$, $Fe(NO_3)_3$, $Fe_2(SO_4)_3$, FeS, $FeCl_2$, $FeSO_4$, and metallic Fe(Fe^0) occurred primarily as minor phases (*e.g.*, <50%) in the ash samples. The combustion of vegetation and structural materials produces heat and emissions in the form of water, organic vapors, gases, and particulates. Gaseous emissions include carbon monoxide (CO), carbon dioxide (CO_2), sulfur oxides (SO_x), nitrogen oxides (NO_x), and hydrogen chloride (HCl). These gases react with iron forming various iron compounds (*e.g.*, FeS, $FeCl_2$, $FeCl_3$, $FeSO_4$, and $Fe_2(SO_4)_3$ as observed by XANES).

Maghemite and magnetite were the most frequently detected Fe phases in the ash samples (Table 1). Maghemite,

Table 1 Number of ash and soil samples containing a given phase based on ash source

Phase	All ash	Structural ash	Vegetation ash	Vehicle ash	Atmospheric deposition	Soil
Maghemite	42	30	6	5	1	5
Magnetite	38	23	7	7	0	0
Ferrihydrite	15	10	2	3	1	2
FeS	12	8	0	4	0	0
$FeCl_2$	11	7	3	1	0	2
$FeSO_4$	11	9	0	1	1	0
Goethite	8	5	1	2	0	2
$FeCl_3$	8	4	2	2	0	3
Hematite	5	2	2	1	0	3
Wüstite (FeO)	4	2	0	2	0	0
Fe^0	3	3	0	0	0	0
$Fe(NO_3)_3$	1	0	1	0	0	0
$Fe_2(SO_4)_3$	1	1	0	0	0	0

ferrihydrite, goethite, hematite, $FeCl_3$, and $FeCl_2$ were detected in fire ash as well as soil samples. In contrast, magnetite, FeS, $FeSO_4$, $Fe_2(SO_4)_3$, $Fe(NO_3)_3$, wüstite (FeO), and Fe^0 were not detected in any of the five soil samples investigated in this study, suggesting that these phases formed due to material combustion in fires at the WUI. Sulfur-containing iron phases were not detected in any of the vegetation ash suggesting that these phases formed as a result of the combustion of sulfur-containing materials in structures and vehicles. Notably, these phases could be present in vegetation ash in small amounts. However, one of the intrinsic limitations of LCF is the error associated with this mathematical method and the resolution of the XANES spectra. It is commonly accepted in the XAS scientific community that species with mass below 10% of sample mass do not strongly affect the shape of the fit, and thus cannot be considered as part of the sample.[56,57]

Considering fire severity, indicated by ash color (Fig. 6, S5 and S6†), the majority of ash samples collected from low and medium burn-severity fires (11 out of 13 black ashes, 10 out of 11 gray ashes, and 5 out of 6 brown/gray ashes) contained magnetite. In contrast, a lower proportion of ashes collected from high burn-severity fires (10 out of 16 white ashes) contained magnetite (Table 2). Note that ash classification by color was performed by the naked eye, and that some of the white ashes contained light gray particles. This might explain why some white ashes contained magnetite. Considering the abundance of magnetite as a function of the color of the ash, we found that the relative abundance of magnetite decreased from black to gray to gray/brown to white to green ashes and was absent in red/brown ashes (Fig. 6a and S6a†). Conversely, the relative abundance of maghemite increased from black and gray to gray/brown and white to green, and red/brown (Fig. 6a and S6a†). In short, increasing fire severity was correlated with a decrease in magnetite and an increase in maghemite abundance. In addition, four gray ash samples contained wüstite, and three white ash samples contained metallic Fe. Comparing the iron oxidation states based on the ash color (Fig. 6b and S6b†), Fe^{3+} increased from gray to black and gray/brown to white, green, and red/brown ashes (Fig. 6b), Fe^{3+}/Fe^{2+} decreased following the same trend as magnetite (Fig. 6b), and Fe^{2+} did not display a specific trend with ash color (Fig. 6b). Iron speciation did not display a specific trend as a function of the ash source (Fig. S7†).

The concentration of iron phases in the ashes was estimated using the total Fe concentration and the spectral weight obtained by LCF XANES assuming that the spectral weight of the different phases corresponds to the relative abundance of phase mass within the ashes (Fig. S6†). Most ash samples contained high magnetite levels (*e.g.*, up to 25 mg g^{-1} in fire ash, 18 mg g^{-1} in atmospherically deposited ash, Fig. 7). Magnetite concentrations decreased from black to gray to white ash. These concentrations are much higher than those reported in roadside dust (*e.g.*, 1.8 to 9.5 mg g^{-1})[58] or atmospheric particles (*e.g.*, 0.6 to 13.0 mg g^{-1}).[59–61] The concentration of wüstite varied between 2.4 and 23 mg g^{-1},

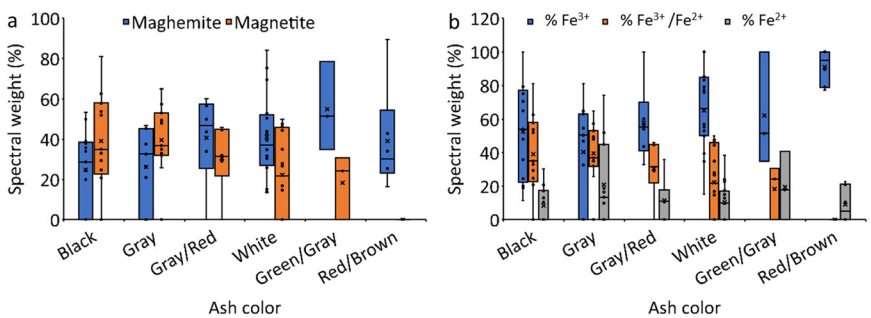

Fig. 6 The spectral weight (%) of (a) magnetite and maghemite, and (b) iron oxidation state in ash and soil samples organized by ash color.

Table 2 Number of ash samples containing a given phase based on ash color

Phase	Black	Gray	Gray/brown	White	Gray/green	Red
Total number of ashes	13	11	6	16	3	6
Maghemite	9	8	5	16	3	6
Magnetite	11	10	5	10	2	0
Ferrihydrite	5	3	1	6	0	2
FeS	2	4	0	5	1	0
$FeCl_2$	2	2	1	5	0	3
$FeSO_4$	2	3	3	2	1	0
Goethite	3	2	1	2	0	2
$FeCl_3$	2	2	0	3	1	3
Hematite	3	0	1	1	0	3
Wüstite (FeO)	0	2	1	0	1	0
Fe^0	0	0	0	3	0	0
$Fe(NO_3)_3$	1	0	0	0	0	0
$Fe_2(SO_4)_3$	0	0	0	1	0	0

whereas the concentration of metallic Fe varied between 0.9 and 2.4 mg g^{-1} (Fig. S8†). The concentrations of metallic Fe in road dust are relatively low (~0.15 mg g^{-1}).[58]

The relative abundance of the different oxidation states of Fe and the phases themselves in the WUI ash samples are presented in Fig. 6b and S6b.† The oxidized Fe^{3+} components were the dominant type in most ash samples and represented 0 to 100% of the total normalized Fe spectral signal (Fig. 6b). The mixed Fe^{3+}/ Fe^{2+} phases represented 0 to 81%, the reduced Fe^{2+} represented 0 to 98%, and the most reduced Fe^0 represented 0 to 14%. In contrast, in the soil samples, oxidized Fe^{3+} accounted for 77 to 100% and Fe^{2+} accounted for only 0 to 23% of the total normalized Fe spectral signal.

4. Discussion

XANES analyses revealed that the dominant iron phases in the soil samples investigated in this study were ferrihydrite, goethite, maghemite, hematite, $FeCl_2$, and $FeCl_3$. Iron oxyhydroxides such as ferrihydrite, goethite, lepidocrocite (γ-$Fe^{3+}OOH$), and hematite were the major forms of iron in soils as products of weathering reactions of the soil parent.[62] In contrast, vegetation, structure, and vehicle ashes were dominated by ferromagnetic (*i.e.*, magnetically ordered) minerals, especially magnetite and maghemite. Other Fe-bearing phases were also detected in these ashes, including hematite, wüstite, and metallic Fe. These findings suggest that magnetite, wüstite, and metallic Fe formed due to the combustion of materials during fires at the WUI.

Iron oxide NPs undergo various transformations during material combustion, which depend on the fire redox conditions. For instance, hematite is resistant to transformation at high temperature under oxidizing conditions. In contrast, under reducing conditions, hematite can be converted to maghemite or magnetite. Heat treatment of hematite and goethite in the presence of a reducing agent (5 wt% starch, $(C_6H_{10}O_5)_n$) leads to their conversion into magnetite. This transformation starts at 300 to 350 °C and increases with temperature,[63–65] then the transformation rate decelerates at approximately 500 °C.[63] Hematite transforms to maghemite or magnetite in the presence of organic matter at temperatures >450 °C.[66] This transformation is caused by the partial reduction of Fe^{3+} to Fe^{2+} by carbon and the subsequent formation of maghemite and magnetite. Thermal treatment of lepidocrocite under oxidizing conditions leads to the formation of maghemite at 250 °C, which then starts to transform to hematite at 350 °C. In contrast, thermal treatment of lepidocrocite under reducing conditions leads to the formation of magnetite through the intermediate formation of maghemite and hematite. These transformations start at 200 to 250 °C and continue up to 900 °C.[67,68] When heated under oxidizing conditions, goethite transforms to hematite. In contrast, when heated under reducing conditions, goethite (natural coarse particles of goethite iron ore) transforms to magnetite with possible intermediate hematite formation.[2,69–71] In the presence of glucose, goethite begins to transform to a high-magnetic mineral at 450 °C.[66] The reduction of synthetic and brown goethite results in the formation of magnetite at 270 °C and 500 °C, respectively.[72] Therefore, temperature and redox conditions are expected to be the most important factors

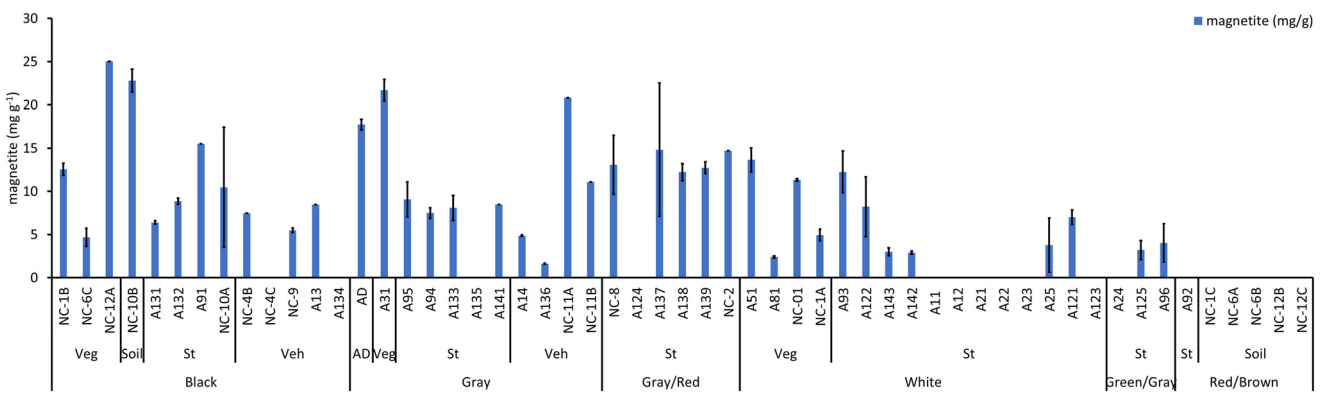

Fig. 7 Magnetite concentration (mg g^{-1}) in ash generated as a result of fires at the wildland–urban interface as a function of ash color and fuel source. Veg: vegetation, St: structure, Veh: vehicle, and AD: atmospheric deposition.

controlling the transformations of iron oxides in the case of fire events in the WUI.

The pyrolysis of biomass (*e.g.*, pine tree biomass, palm oil waste) and structural material (*e.g.*, wood) generates heat, CO, H_2, and black carbon, which act as heating and reducing agents for the reduction of iron oxide.[2,3] The CO, H_2, and black carbon reductants cause the reduction process through a series of interrelated reactions (eqn (1)–(6)).[73,74] The complete reduction of iron oxides consists of the reduction of iron oxides (*e.g.*, hematite, goethite, lepidocrocite) to magnetite, magnetite to wüstite, and wüstite to metallic iron. The degree of iron oxide reduction is determined by the reduction temperature, reaction time, and air/biomass ratio.[2]

$$3Fe_2O_3 + CO \rightarrow 2Fe_3O_4 + CO_2 \quad (1)$$

$$Fe_3O_4 + CO \rightarrow 3FeO + CO_2 \quad (2)$$

$$FeO + CO \rightarrow Fe + CO_2 \quad (3)$$

$$3Fe_2O_3 + H_2 \rightarrow 2Fe_3O_4 + H_2O \quad (4)$$

$$Fe_3O_4 + H_2 \rightarrow 3FeO + H_2O \quad (5)$$

$$FeO + H_2 \rightarrow Fe + H_2O \quad (6)$$

Depending on the availability of excess carbon and hydrogen, the reduction follows the above stepwise mechanism during fires at the WUI. Increases in reduction temperature, reaction time, the concentration of the reducing agent (*e.g.*, CO, H_2, black carbon), as well as the decrease in iron oxide particle size favor the reduction of iron oxides (*e.g.*, goethite, hematite, lepidocrocite) to magnetite, wüstite, and finally metallic iron.[63,73]

The lower relative abundance of magnetite in white ashes (*e.g.*, high-fire severity) could be due to (i) the transformation of magnetite to the more reduced iron oxide phases at higher fire severity, which is supported by the detection of wüstite in gray ashes and Fe^0 in white ashes (Table 2); (ii) the decrease in the reducing agent (electron acceptor) concentrations under high-fire severity conditions; and/or (iii) the oxidative transformations of reduced iron phases to the oxidized forms (*e.g.*, maghemite and hematite) due to a change in the environmental redox conditions. Under low-fire severity (*i.e.*, <450 °C) conditions, carbon is not completely oxidized, which generates CO and/or black carbon. In contrast, high intensity fires (>450 °C) produce CO_2, H_2O, and light gray or white ashes composed of mainly alkaline oxides (Ca, K, Mg oxides).[75] The total amount and duration of CO emissions decrease with increases in combustion temperature due to increased combustion completeness.[76] Additionally, the amount of emitted CO and black carbon depends on the type of burned biomass or structural material. These conditions might limit the reduction of iron oxides under high-fire severity. On the other hand, newly formed magnetite (by reduction of hematite in the presence of starch or other organic matter) could re-oxidize to maghemite at temperatures >600 °C due to changes in reducing and oxidizing conditions (*i.e.*, consumption of starch during the reduction reaction).[2,63,77] In contrast, at low fire severity black carbon could prevent the reoxidation of reduced iron oxides.[78]

5. Implications for public health and global warming

This study reveals that wildfires at the WUI can convert iron oxides to reduced iron phases such as magnetite, wüstite, and zero-valent iron. We found that magnetite concentrations (up to 25 mg g^{-1} of ash) in deposited and atmospherically transported ash are higher than those reported in typical atmospheric and roadside particles. These findings provide important information for understanding the potential health risks, environmental impacts, and global warming implications of wildfires at the WUI, all of which remain poorly understood.

In terms of public health risks, wildfires, wood smoke, and magnetite exposures have been associated with neurodegenerative diseases such as cognitive dysfunction, including Alzheimer's disease and dementia.[17,18,35,36,79] Considering the potential neurotoxicity of magnetite particles and the abundance of magnetite NPs in wildfire emissions, it is reasonable to speculate that magnetite particles emitted from fires at the WUI could contribute to the pathogenesis of neurodegenerative diseases, warranting further investigation. This is of particular concern for the entire population of the continental United States and many other countries due to the long-distance transport and related, widespread exposure to wildfire contaminants.

Wildfire smoke is a major source of ambient particulate matter, contributing to as much as 70% of $PM_{2.5}$ in the western United States on days when regulatory limits (10 μg m^{-3}) are exceeded.[80] $PM_{2.5}$ refers to particulate pollutants that are 2.5 micrometers or smaller in size and are associated with the greatest proportion of adverse health effects related to air pollution, including premature mortality, increased hospital admission for heart or lung causes, acute and chronic bronchitis, asthma attacks, emergency room visits, respiratory symptoms, and restricted activity days.[81] The North American annual $PM_{2.5}$ emissions from wildfires are estimated at 1.9 to 2.2 Tg per year,[82] and the total U.S. anthropogenic $PM_{2.5}$ emissions are estimated at 4.1 Tg per year.[83] A multi-year (2013–2016) analysis of wildfire forecasted $PM_{2.5}$ concentrations from burning biomass over North America suggested that on average over the fire season, 69% of United States residents and 76% of Canadian residents were affected by seasonal wildfire-related $PM_{2.5}$ concentrations above 0.2 μg m^{-3}, and these effects were particularly pronounced in July and August.[84] Additionally, fire emissions contributed more than 1 μg m^{-3} of daily average $PM_{2.5}$ concentrations on more than 30% of days in the western United States and northwestern Canada during

the fire season.[84] The 0.2 μg m^{-3} threshold is the threshold above which any annual $PM_{2.5}$ change is considered a non-negligible impact according to the U.S. Environmental Protection Agency (EPA) Significant Impact Level. The 1 μg m^{-3} threshold is considered a transition between the minimal 0.2 μg m^{-3} and the 10 μg m^{-3} threshold.[85] The United States population affected by average seasonal fire-$PM_{2.5}$ > 10 μg m^{-3} ranged from 179 841 to 354 050, with a four-year season average (2013–2016) exposure of 0.1% of the United States population.[84] It is expected that wildfire smoke could generate greater than 50% of total $PM_{2.5}$ for the entire United States by the year 2100.[86] In the present study, unraveling the abundances and properties of magnetite NPs provides a valuable reference for toxicological studies and risk assessment.

In terms of global environmental impacts, a recent study reported anomalously widespread phytoplankton blooms in the Southern Ocean downwind of Australia. These blooms were attributed to the transport of wildfire-generated iron-rich aerosols to the bloom regions, resulting in the fertilization of the iron-limited waters of the Southern Ocean,[37] possibly due to the higher solubility of iron in seawater from combustion sources than that from mineral dust.[87] Yet the role of iron solid phase speciation and mineralogy have not yet been considered. The high relative abundance of Fe^{2+} in fire ashes could play an important role in the bioavailability of iron in the ocean.[38]

In terms of global warming, particulate matter (*e.g.*, black carbon, brown carbon, and mineral dust) has been largely considered as the only significant anthropogenic contributor to shortwave (*e.g.*, 300 to 2500 nm) atmospheric heating.[88] However, anthropogenic iron oxide aerosols have been recently recognized to be significant contributors to shortwave atmospheric heating because iron oxides are strong absorbers at visible wavelengths.[39,89] Iron speciation regulates the light-absorption properties of iron oxides. Magnetite is the most efficient shortwave absorber among the iron oxide minerals in the atmosphere, as the imaginary part of the refractive index for magnetite is similar to that of black carbon.[90,91] The shortwave heating rates by anthropogenic magnetite particles, released from blast furnaces of iron manufacturing facilities and engine and brakes of motor vehicles, were estimated to be at least 4–7, 0.8–7, 0.7–14, and 0.3–26% of that of black carbon in East Asia, the Southern Ocean, the Pacific Ocean, and the Atlantic Ocean, respectively.[39,92] Given their high concentrations, WUI fire-released magnetite may have a climate heating effect through absorption of shortwave solar radiation.[40] We note the discussion above provides only a brief discussion of the global environmental and climatological impacts of iron oxide nanoparticles in fire ashes. A more detailed discussion of the environmental and climatological impacts of iron oxide nanoparticles can be found elsewhere.[6]

Our XANES analyses revealed that strongly magnetic particles (magnetite and maghemite) displayed a higher relative abundance (*e.g.*, 15 to 100% with an average of 65% ± 23 spectral weight) in fire ash relative to those in soils (*e.g.*, 16 to 43% with an average of 29% ± 10 spectral weight). These findings suggest that wildfires contribute to the magnetic enhancement of topsoil as reported elsewhere.[29,93] Understanding the impact of fires on soil magnetism is important for accurate interpretation of magnetic paleoenvironmental proxies.

This study focused on the speciation of Fe-bearing particles in WUI fire ashes. Future studies investigating the solid phase speciation of other metal-bearing particles such as Ti, Cr, and Cu-bearing particles could provide additional valuable insights.

Competing interest statement

The authors declare no competing interest.

Author contributions

Dr. Mohammed Baalousha conceived the overall idea of the research, coordinated the collaboration among the research team, performed data analysis, and wrote the first draft. Dr. Jackson P. Webster, Dr. Sandrine J. Matiasek, and Dr. Charles N. Alpers performed field sampling campaigns and provided extensive background information on the sampling sites and the collected samples. Dr. Morgane Desmau collected the X-ray absorption data and performed data analysis. Dr. Sheryl A. Singerling performed transmission electron microscopy analysis and the associated data analysis. Ms. Michelle A. Stern generated the burn severity and land use maps. All authors contributed to the manuscript writing and editing.

Conflicts of interest

There are no conflicts to declare.

Acknowledgements

This work was supported by a RAPID grant (2101983) from the United States National Science Foundation (NSF) and by the Nanoscale Characterization and Fabrication Laboratory and the Virginia Tech National Center for Earth and Environmental Nanotechnology Infrastructure (NanoEarth), a member of the National Nanotechnology Coordinated Infrastructure (NNCI), supported by NSF (ECCS 1542100 and ECCS 2025151). We acknowledge DESY (Hamburg, Germany), a member of the Helmholtz Association HGF, for the provision of experimental facilities. Parts of this research were carried out at PetraIII, and we would like to thank Edmund Welter and Regina Biller for their assistance in using the beamline P65. We would like to thank Thaïs Couasnon, Jeff P. Perez and Roberts Blukis from the GFZ German Research Center for Geosciences as well as Akhil Tayal and Xiao Sun from DESY, for providing some of the Fe references for XAS analysis and helping with the synthesis of others. Any use of trade, firm, or product names is for descriptive purposes only and does not imply endorsement by the U.S. Government.

Notes and references

1 M. B. Bodí, D. A. Martin, V. N. Balfour, C. Santín, S. H. Doerr, P. Pereira, A. Cerdà and J. Mataix-Solera, Wildland fire ash: production, composition and eco-hydro-geomorphic effects, *Earth-Sci. Rev.*, 2014, **130**, 103–127.

2 Y. Wu, M. Fang, L. Lan, P. Zhang, K. V. Rao and Z. Bao, Rapid and direct magnetization of goethite ore roasted by biomass fuel, *Sep. Purif. Technol.*, 2012, **94**, 34–38.

3 R. Z. A. Rashid, H. M. Salleh, M. H. Ani, N. A. Yunus, T. Akiyama and H. Purwanto, Reduction of low grade iron ore pellet using palm kernel shell, *Renewable Energy*, 2014, **63**, 617–623.

4 Y. Yang, B. Chen, J. Hower, M. Schindler, C. Winkler, J. Brandt, R. Di Giulio, J. Ge, M. Liu, Y. Fu, L. Zhang, Y. Chen, S. Priya and M. F. Hochella, Discovery and ramifications of incidental Magnéli phase generation and release from industrial coal-burning, *Nat. Commun.*, 2017, **8**, 194.

5 D. K. McDaniel, V. M. Ringel-Scaia, H. A. Morrison, S. Coutermarsh-Ott, M. Council-Troche, J. W. Angle, J. B. Perry, G. Davis, W. Leng and V. Minarchick, Pulmonary exposure to Magnéli phase titanium suboxides results in significant macrophage abnormalities and decreased lung function, *Front. Immunol.*, 2019, **10**, 2714.

6 M. F. Hochella, D. W. Mogk, J. Ranville, I. C. Allen, G. W. Luther, L. C. Marr, B. P. McGrail, M. Murayama, N. P. Qafoku and K. M. Rosso, Natural, incidental, and engineered nanomaterials and their impacts on the Earth system, *Science*, 2019, **363**(6434), eaau8299.

7 R. J. Bixby, S. D. Cooper, R. E. Gresswell, L. E. Brown, C. N. Dahm and K. A. Dwire, Fire effects on aquatic ecosystems: an assessment of the current state of the science, *Freshw. Sci.*, 2015, **34**, 1340–1350.

8 J. D. Miller, H. Safford, M. Crimmins and A. E. Thode, Quantitative evidence for increasing forest fire severity in the Sierra Nevada and southern Cascade Mountains, California and Nevada, USA, *Ecosystems*, 2009, **12**, 16–32.

9 H. Chen, A. T. Chow, X.-W. Li, H.-G. Ni, R. A. Dahlgren, H. Zeng and J.-J. Wang, Wildfire burn intensity affects the quantity and speciation of polycyclic aromatic hydrocarbons in soils, *ACS Earth Space Chem.*, 2018, **2**, 1262–1270.

10 M. Scholze, W. Knorr, N. W. Arnell and I. C. Prentice, A climate-change risk analysis for world ecosystems, *Proc. Natl. Acad. Sci. U. S. A.*, 2006, **103**, 13116–13120.

11 K. D. Bladon, M. B. Emelko, U. Silins and M. Stone, Wildfire and the future of water supply, *Environ. Sci. Technol.*, 2014, **48**(16), 8936–8943.

12 D. Q. Brito, C. J. S. Passos, D. H. Muniz and E. C. Oliveira-Filho, Aquatic ecotoxicity of ashes from Brazilian savanna wildfires, *Environ. Sci. Pollut. Res.*, 2017, **24**, 19671–19682.

13 T. C. Wegesser, K. E. Pinkerton and J. A. Last, California wildfires of 2008: coarse and fine particulate matter toxicity, *Environ. Health Perspect.*, 2009, **117**, 893–897.

14 Y. H. Kim, S. H. Warren, Q. T. Krantz, C. King, R. Jaskot, W. T. Preston, B. J. George, M. D. Hays, M. S. Landis and M. Higuchi, Mutagenicity and lung toxicity of smoldering vs. flaming emissions from various biomass fuels: implications for health effects from wildland fires, *Environ. Health Perspect.*, 2018, **126**, 017011.

15 R. Aguilera, T. Corringham, A. Gershunov and T. Benmarhnia, Wildfire smoke impacts respiratory health more than fine particles from other sources: observational evidence from Southern California, *Nat. Commun.*, 2021, **12**, 1493.

16 J. C. Liu, A. Wilson, L. J. Mickley, F. Dominici, K. Ebisu, Y. Wang, M. P. Sulprizio, R. D. Peng, X. Yue and J.-Y. Son, Wildfire-specific fine particulate matter and risk of hospital admissions in urban and rural counties, *Epidemiology*, 2017, **28**, 77.

17 A. Schuller and L. Montrose, Influence of Woodsmoke Exposure on Molecular Mechanisms Underlying Alzheimer's Disease: Existing Literature and Gaps in Our Understanding, *Epigenetics Insights*, 2020, **13**, 2516865720954873.

18 A. Oudin, D. Segersson, R. Adolfsson and B. Forsberg, Association between air pollution from residential wood burning and dementia incidence in a longitudinal study in Northern Sweden, *PLoS One*, 2018, **13**, e0198283.

19 E. Ormeno, B. Cespedes, I. A. Sanchez, A. Velasco-García, J. M. Moreno, C. Fernandez and V. Baldy, The relationship between terpenes and flammability of leaf litter, *For. Ecol. Manage.*, 2009, **257**, 471–482.

20 S. Saura-Mas, S. Paula, J. Pausas and F. Lloret, Fuel loading and flammability in the Mediterranean Basin woody species with different post-fire regenerative strategies, *Int. J. Wildland Fire*, 2010, **19**, 783–794.

21 L. F. DeBano, D. G. Neary and P. F. Ffolliott, *Fire effects on ecosystems*, John Wiley & Sons, 1998.

22 T. Horie, F. Hauser and J. I. Schroeder, HKT transporter-mediated salinity resistance mechanisms in Arabidopsis and monocot crop plants, *Trends Plant Sci.*, 2009, **14**, 660–668.

23 J. L. Jambor and J. E. Dutrizac, Occurrence and constitution of natural and synthetic ferrihydrite, a widespread iron oxyhydroxide, *Chem. Rev.*, 1998, **98**, 2549–2586.

24 M. Gajdardziska-Josifovska, R. G. McClean, M. A. Schofield, C. V. Sommer and W. F. Kean, Discovery of nanocrystalline botanical magnetite, *Eur. J. Mineral.*, 2001, **13**, 863–870.

25 R. G. McClean and W. F. Kean, Contributions of wood ash magnetism to archaeomagnetic properties of fire pits and hearths, *Earth Planet. Sci. Lett.*, 1993, **119**, 387–394.

26 J. A. Ober, Mineral resource of the month: Iron oxide pigments, *Earth Magazine*, 2008.

27 United States Geological Survey, *Mineral commodity summaries 2021*, 2021, p. 200, DOI: **10.3133/mcs2021**.

28 G. P. Mastrotheodoros and K. G. Beltsios, Pigments—Iron-based red, yellow, and brown ochres, *Archaeol. Anthropol. Sci.*, 2022, **14**, 35.

29 J. L. Till, B. Moskowitz and S. W. Poulton, Magnetic properties of plant ashes and their influence on magnetic signatures of fire in soils, *Front. Earth Sci.*, 2021, **8**, 592659.

30 N. Jordanova, D. Jordanova and V. Barrón, Wildfire severity: Environmental effects revealed by soil magnetic properties, *Land Degrad. Dev.*, 2019, **30**, 2226–2242.

31 B. A. Maher, I. A. M. Ahmed, V. Karloukovski, D. A. MacLaren, P. G. Foulds, D. Allsop, D. M. A. Mann, R. Torres-Jardón and L. Calderon-Garciduenas, Magnetite pollution nanoparticles in the human brain, *Proc. Natl. Acad. Sci. U. S. A.*, 2016, **113**, 10797–10801.

32 D. Lu, Q. Luo, R. Chen, Y. Zhuansun, J. Jiang, W. Wang, X. Yang, L. Zhang, X. Liu, F. Li, Q. Liu and G. Jiang, Chemical multi-fingerprinting of exogenous ultrafine particles in human serum and pleural effusion, *Nat. Commun.*, 2020, **11**, 2567.

33 L. Calderón-Garcidueñas, A. González-Maciel, P. S. Mukherjee, R. Reynoso-Robles, B. Pérez-Guillé, C. Gayosso-Chávez, R. Torres-Jardón, J. V. Cross, I. A. M. Ahmed, V. V. Karloukovski and B. A. Maher, Combustion- and friction-derived magnetic air pollution nanoparticles in human hearts, *Environ. Res.*, 2019, **176**, 108567.

34 M. Könczöl, S. Ebeling, E. Goldenberg, F. Treude, R. Gminski, R. Gieré, B. Grobéty, B. Rothen-Rutishauser, I. Merfort and V. Mersch-Sundermann, Cytotoxicity and Genotoxicity of Size-Fractionated Iron Oxide (Magnetite) in A549 Human Lung Epithelial Cells: Role of ROS, JNK, and NF-κB, *Chem. Res. Toxicol.*, 2011, **24**, 1460–1475.

35 Q. Pankhurst, D. Hautot, N. Khan and J. Dobson, Increased Levels of Magnetic Iron Compounds in Alzheimer's Disease, *J. Alzheimer's Dis.*, 2008, **13**, 49–52.

36 D. Hautot, Q. A. Pankhurst, N. Khan and J. Dobson, Preliminary evaluation of nanoscale biogenic magnetite in Alzheimer's disease brain tissue, *Proc. R. Soc. London, Ser. B*, 2003, **270**, S62–S64.

37 W. Tang, J. Llort, J. Weis, M. M. G. Perron, S. Basart, Z. Li, S. Sathyendranath, T. Jackson, E. S. Rodriguez, B. C. Proemse, A. R. Bowie, C. Schallenberg, P. G. Strutton, R. Matear and N. Cassar, Widespread phytoplankton blooms triggered by 2019–2020 Australian wildfires, *Nature*, 2021, **597**, 370–375.

38 A. Ito, Y. Ye, C. Baldo and Z. Shi, Ocean fertilization by pyrogenic aerosol iron, *npj Clim. Atmos. Sci.*, 2021, **4**, 30.

39 N. Moteki, K. Adachi, S. Ohata, A. Yoshida, T. Harigaya, M. Koike and Y. Kondo, Anthropogenic iron oxide aerosols enhance atmospheric heating, *Nat. Commun.*, 2017, **8**, 1–11.

40 H. Matsui, N. M. Mahowald, N. Moteki, D. S. Hamilton, S. Ohata, A. Yoshida, M. Koike, R. A. Scanza and M. G. Flanner, Anthropogenic combustion iron as a complex climate forcer, *Nat. Commun.*, 2018, **9**, 1593–1593.

41 inciweb, *Incident information system: North Complex*, 2022, **https://inciweb.nwcg.gov/incident/6997/**.

42 United States Department of Agriculture, *Burned-area report: North complex*, Report FS-2500-8 (2/20), United States Department of Agriculture Forest Service, 2020.

43 CALFire, *LNU Lightning Complex (includes Hennessey, Gamble, 15-10, Spanish, Markley, 13-4, 11-16, Walbridge) Incident*, 2022, **https://www.fire.ca.gov/incidents/2020/8/17/lnu-lightning-complex-includes-hennessey-gamble-15-10-spanish-markley-13-4-11-16-walbridge/**.

44 E. Welter, R. Chernikov, M. Herrmann and R. Nemausat, A beamline for bulk sample x-ray absorption spectroscopy at the high brilliance storage ring PETRA III, *AIP Conf. Proc.*, 2019, **2054**, 040002.

45 M. Newville, Larch: an analysis package for XAFS and related spectroscopies, *J. Phys.: Conf. Ser.*, 2013, **430**, 012007.

46 M. Desmau, A python library to read, process and analyze X-ray absorption spectra, **https://github.com/marcoalsina/araucaria**.

47 S. Van Der Walt, S. C. Colbert and G. Varoquaux, The NumPy array: a structure for efficient numerical computation, *Comput. Sci. Eng.*, 2011, **13**, 22–30.

48 P. Virtanen, R. Gommers, T. E. Oliphant, M. Haberland, T. Reddy, D. Cournapeau, E. Burovski, P. Peterson, W. Weckesser and J. Bright, SciPy 1.0: fundamental algorithms for scientific computing in Python, *Nat. Methods*, 2020, **17**, 261–272.

49 J. D. Hunter, Matplotlib: A 2D graphics environment, *Comput. Sci. Eng.*, 2007, **9**, 90–95.

50 U. Schwertmann and R. M. Cornell, *Iron oxides in the laboratory: preparation and characterization*, John Wiley & Sons, 2008.

51 U. Schwertmann, P. Cambier and E. Murad, Properties of goethites of varying crystallinity, *Clays Clay Miner.*, 1985, **33**, 369–378.

52 M. Desmau, M. A. Alsina and J.-F. Gaillard, XAS study of Sn speciation in toothpaste, *J. Anal. At. Spectrom.*, 2021, **36**, 407–415.

53 C. Da Silva-Cadoux, L. Zanella and J.-F. Gaillard, Selecting reference compounds for determining chemical speciation by X-ray absorption spectroscopy, *J. Anal. At. Spectrom.*, 2012, **27**, 957–965.

54 M. Newville, T. Stensitzki, D. B. Allen, M. Rawlik, A. Ingargiola and A. Nelson, LMFIT: Non-linear least-square minimization and curve-fitting for Python, *Astrophysics Source Code Library*, 2016, ascl, p. 1606.1014.

55 J. G. Chen, NEXAFS investigations of transition metal oxides, nitrides, carbides, sulfides and other interstitial compounds, *Surf. Sci. Rep.*, 1997, **30**, 1–152.

56 E. Doelsch, I. Basile-Doelsch, J. Rose, A. Masion, D. Borschneck, J.-L. Hazemann, H. Saint Macary and J.-Y. Bottero, New combination of EXAFS spectroscopy and density fractionation for the speciation of chromium within an andosol, *Environ. Sci. Technol.*, 2006, **40**, 7602–7608.

57 M. Munoz, V. De Andrade, O. Vidal, E. Lewin, S. Pascarelli and J. Susini, Redox and speciation micromapping using dispersive X-ray absorption spectroscopy: Application to iron in chlorite mineral of a metamorphic rock thin section, *Geochem., Geophys., Geosyst.*, 2006, **7**, Q11020.

58 T. Gonet, B. A. Maher and J. Kukutschová, Source apportionment of magnetite particles in roadside airborne particulate matter, *Sci. Total Environ.*, 2021, **752**, 141828.

59 A. R. Muxworthy, J. Matzka, A. F. Davila and N. Petersen, Magnetic signature of daily sampled urban atmospheric particles, *Atmos. Environ.*, 2003, **37**, 4163–4169.

60 A. R. Muxworthy, J. Matzka and N. Petersen, Comparison of magnetic parameters of urban atmospheric particulate

matter with pollution and meteorological data, *Atmos. Environ.*, 2001, **35**, 4379–4386.
61 Q. Zhang, D. Lu, D. Wang, X. Yang, P. Zuo, H. Yang, Q. Fu, Q. Liu and G. Jiang, Separation and Tracing of Anthropogenic Magnetite Nanoparticles in the Urban Atmosphere, *Environ. Sci. Technol.*, 2020, **54**, 9274–9284.
62 U. Schwertmann, Occurrence and formation of iron oxides in various pedoenvironments, in *Iron in soils and clay minerals*, D. Reidek Publishing Company, Boston, 1988, vol. 11, pp. 267–308.
63 V. P. Ponomar, T. S. Antonenko, O. A. Vyshnevskyi and A. B. Brik, Thermally induced changes in the magnetic properties of iron oxide nanoparticles under reducing and oxidizing conditions, *Adv. Powder Technol.*, 2020, **31**, 2587–2596.
64 M. S. Ellid, Y. S. Murayed, M. S. Zoto, S. Musić and S. Popović, Chemical reduction of hematite with starch, *J. Radioanal. Nucl. Chem.*, 2003, **258**, 299–305.
65 V. P. Ponomar, N. O. Dudchenko and A. B. Brik, Reduction roasting of hematite to magnetite using carbohydrates, *Int. J. Miner. Process.*, 2017, **164**, 21–25.
66 M. Hanesch, H. Stanjek and N. Petersen, Thermomagnetic measurements of soil iron minerals: the role of organic carbon, *Geophys. J. Int.*, 2006, **165**, 53–61.
67 A. Gehring and A. Hofmeister, The transformation of lepidocrocite during heating: a magnetic and spectroscopic study, *Clays Clay Miner.*, 1994, **42**, 409–415.
68 T. S. Gendler, V. P. Shcherbakov, M. J. Dekkers, A. K. Gapeev, S. K. Gribov and E. McClelland, The lepidocrocite–maghemite–haematite reaction chain—I. Acquisition of chemical remanent magnetization by maghemite, its magnetic properties and thermal stability, *Geophys. J. Int.*, 2005, **160**, 815–832.
69 M. Valix and W. Cheung, Study of phase transformation of laterite ores at high temperature, *Miner. Eng.*, 2002, **15**, 607–612.
70 Q. Y. Wang, Y. Wu, Y. H. Li and X. Yang, Biomass reduction roasting-magnetic separation of low grade goethite, *Mater. Sci. Forum*, 2015, **814**, 235–240.
71 W. Cheung and M. Valix, Selective Reduction Roasting of Limonite Ores: Effect of Over-reduction, *Proceedings of XXIV International Mineral Processing Congress*, 2008, pp. 2951–2957.
72 V. P. Ponomar, Thermomagnetic properties of the goethite transformation during high-temperature treatment, *Miner. Eng.*, 2018, **127**, 143–152.
73 S. Luo, C. Yi and Y. Zhou, Direct reduction of mixed biomass-Fe2O3 briquettes using biomass-generated syngas, *Renewable Energy*, 2011, **36**, 3332–3336.
74 M. Kumar, S. Nath and S. K. Patel, Studies on the reduction–swelling behaviors of hematite iron ore pellets with noncoking coal, *Miner. Process. Extr. Metall. Rev.*, 2010, **31**, 256–268.
75 D. T. Gottuk, R. J. Roby and C. L. Beyler, The role of temperature on carbon monoxide production in compartment fires, *Fire Saf. J.*, 1995, **24**, 315–331.
76 Q. Xu, W. Peng and C. Ling, An experimental analysis of soybean straw combustion on both CO and NOx emission characteristics in a tubular furnace, *Energies*, 2020, **13**, 1587.
77 K. Przepiera and A. Przepiera, Kinetics of thermal transformations of precipitated magnetite and goethite, *J. Therm. Anal. Calorim.*, 2001, **65**, 497–503.
78 M. J. Molaei, A. Ataie, S. Raygan and S. J. Picken, The effect of different carbon reducing agents in synthesizing barium ferrite/magnetite nanocomposites, *Mater. Chem. Phys.*, 2018, **219**, 155–161.
79 B. A. Maher, Airborne magnetite-and iron-rich pollution nanoparticles: potential neurotoxicants and environmental risk factors for neurodegenerative disease, including Alzheimer's disease, *J. Alzheimer's Dis.*, 2019, **71**, 361–375.
80 J. C. Liu, L. J. Mickley, M. P. Sulprizio, F. Dominici, X. Yue, K. Ebisu, G. B. Anderson, R. F. A. Khan, M. A. Bravo and M. L. Bell, Particulate air pollution from wildfires in the Western US under climate change, *Clim. Change*, 2016, **138**, 655–666.
81 S. Sharma, M. Chandra and S. H. Kota, Health Effects Associated with PM2.5: a Systematic Review, *Curr. Pollut. Rep.*, 2020, **6**, 345–367.
82 J. Kaiser, A. Heil, M. Andreae, A. Benedetti, N. Chubarova, L. Jones, J.-J. Morcrette, M. Razinger, M. Schultz and M. Suttie, Biomass burning emissions estimated with a global fire assimilation system based on observed fire radiative power, *Biogeosciences*, 2012, **9**, 527–554.
83 J. Xing, J. Pleim, R. Mathur, G. Pouliot, C. Hogrefe, C.-M. Gan and C. Wei, Historical gaseous and primary aerosol emissions in the United States from 1990 to 2010, *Atmos. Chem. Phys.*, 2013, **13**, 7531–7549.
84 R. Munoz-Alpizar, R. Pavlovic, M. D. Moran, J. Chen, S. Gravel, S. B. Henderson, S. Ménard, J. Racine, A. Duhamel and S. Gilbert, Multi-year (2013–2016) PM2. 5 wildfire pollution exposure over North America as determined from operational air quality forecasts, *Atmosphere*, 2017, **8**, 179.
85 United States Environmental Protection Agency, *Draft Guidance for Comment: Significant Impact Levels for Ozone and Fine Particle in the Prevention of Significant Deterioration Permitting Program, 2016*, p. 13. Available online: **https://www.epa.gov/sites/production/files/2016-08/documents/pm2_5_sils_and_ozone_draft_guidance.pdf** (accessed on 18 February 2022), 2016.
86 B. Ford, M. Val Martin, S. Zelasky, E. Fischer, S. Anenberg, C. L. Heald and J. Pierce, Future fire impacts on smoke concentrations, visibility, and health in the contiguous United States, *GeoHealth*, 2018, **2**, 229–247.
87 P. N. Sedwick, E. R. Sholkovitz and T. M. Church, Impact of anthropogenic combustion emissions on the fractional solubility of aerosol iron: Evidence from the Sargasso Sea, *Geochem., Geophys., Geosyst.*, 2007, **8**, Q10Q06.
88 B. H. Samset, C. W. Stjern, E. Andrews, R. A. Kahn, G. Myhre, M. Schulz and G. L. Schuster, Aerosol Absorption: Progress Towards Global and Regional Constraints, *Curr. Clim. Change Rep.*, 2018, **4**, 65–83.

89 C. Baldo, P. Formenti, S. Nowak, S. Chevaillier, M. Cazaunau, E. Pangui, C. Di Biagio, J. F. Doussin, K. Ignatyev, P. Dagsson-Waldhauserova, O. Arnalds, A. R. MacKenzie and Z. Shi, Distinct chemical and mineralogical composition of Icelandic dust compared to northern African and Asian dust, *Atmos. Chem. Phys.*, 2020, **20**, 13521–13539.
90 R. W. Bergstrom Jr, Predictions of the spectral absorption and extinction coefficients of an urban air pollution aerosol model, *Atmos. Environ.*, 1972, **6**, 247–258.
91 J. M. Greenberg and H. C. van de Hulst, *Interstellar dust and related topics*, Springer Science & Business Media, 2012.
92 K. D. Lamb, H. Matsui, J. M. Katich, A. E. Perring, J. R. Spackman, B. Weinzierl, M. Dollner and J. P. Schwarz, Global-scale constraints on light-absorbing anthropogenic iron oxide aerosols, *npj Clim. Atmos. Sci.*, 2021, **4**, 15.
93 G. Kletetschka and S. K. Banerjee, Magnetic stratigraphy of Chinese loess as a record of natural fires, *Geophys. Res. Lett.*, 1995, **22**, 1341–1343.